

Autonomous Interfacial Assembly of Polymer Nanofilms via Surfactant-Regulated Marangoni Instability

Sung-Joon Park,[#] Myung-Seok Lee,[#] Mehmet Emin Kilic,[#] Junil Ryu,[#] Hosik Park, You In Park, Hyoungsoo Kim,^{*} Kwang-Ryeol Lee,^{*} and Jung-Hyun Lee^{*}



Cite This: *Nano Lett.* 2023, 23, 4822–4829



Read Online

ACCESS |



Metrics & More



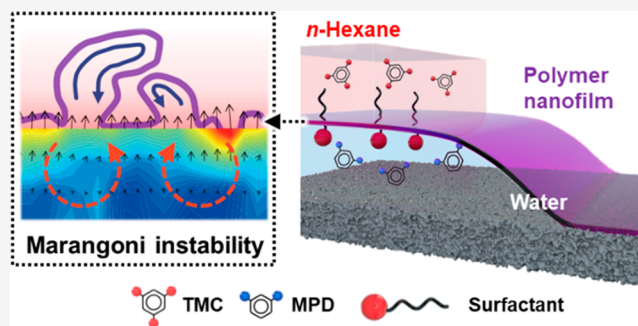
Article Recommendations



Supporting Information

ABSTRACT: Interfacial polymerization (IP) provides a versatile platform for fabricating defect-free functional nanofilms for various applications, including molecular separation, energy, electronics, and biomedical materials. Unfortunately, coupled with complex natural instability phenomena, the IP mechanism and key parameters underlying the structural evolution of nanofilms, especially in the presence of surfactants as an interface regulator, remain puzzling. Here, we interfacially assembled polymer nanofilm membranes at the free water–oil interface in the presence of differently charged surfactants and comprehensively characterized their structure and properties. Combined with computational simulations, an in situ visualization of interfacial film formation discovered the critical role of Marangoni instability induced by the surfactants via various mechanisms in structurally regulating the nanofilms. Despite their different instability-triggering mechanisms, the delicate control of the surfactants enabled the fabrication of defect-free, ultra-permeable nanofilm membranes. Our study identifies critical IP parameters that allow us to rationally design nanofilms, coatings, and membranes for target applications.

KEYWORDS: interfacial polymerization, surfactants, polymer nanofilms, membranes, instability



Due to its highly confined nature, an interface can serve as a versatile platform for assembling functional nanomaterials with unique properties that are unattainable by bulk synthesis.^{1,2} Particularly, interfacial polymerization (IP) occurring at an immiscible liquid–liquid interface offers a facile route to fabricate uniform and defect-free polymer nanofilms for various academic and industrial applications, including sensors, electronics, batteries, catalysts, drug carriers, and separation membranes.^{1,2} Meanwhile, the interface is a fascinating research subject due to spontaneous instability phenomena, which are ubiquitous in nature such as wrinkles of skins and fruits and tears of wine. Many scientists and engineers have sought to understand the fundamentals underlying instability generation and harness interface instability in structuring materials.^{3,4} Unfortunately, the interface instability is a complex natural process, making the governing mechanisms and key structure-regulating parameters for the interfacial formation of nanomaterials puzzling.

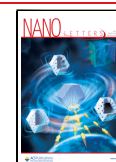
Specifically, IP has evolved as a standard method for commercially producing polyamide (PA) nanofilm membranes for water and organic solvent purification.^{5–12} In practice, a porous support is sequentially immersed in an amine monomer (e.g., *m*-phenylenediamine, MPD) aqueous solution and an acyl chloride monomer organic solution (e.g., trimesoyl chloride [TMC] in *n*-hexane), creating a PA permeable

nanofilm for reverse osmosis (RO) desalination (Figure S1A). Despite the significant technical progress of IP, how the PA nanofilm structure is formed and controlled by synthesis conditions remains obscure, which hampers the precise control and rational design of the polymer nanofilms.^{1,2,13} Particularly, as in many liquid–liquid IP reactions, various surfactants are added to the liquid media to regulate the structure and properties of the PA nanofilms.^{12,14,15} The addition of surfactants has often improved the separation performance of the PA nanofilm. However, the origins of its improved performance associated with its altered structures are still controversial because they were explained by different mechanisms, promoted monomer diffusion, improved support wettability, or their combination.^{12,14,15} Furthermore, combined with the unclear IP mechanism underlying PA film formation,^{1,2,13,16} many contradictory observations of the influence of surfactants on the performance of PA nanofilms^{14,15,17} make a clear identification of the surfactant-

Received: January 30, 2023

Revised: May 9, 2023

Published: May 31, 2023



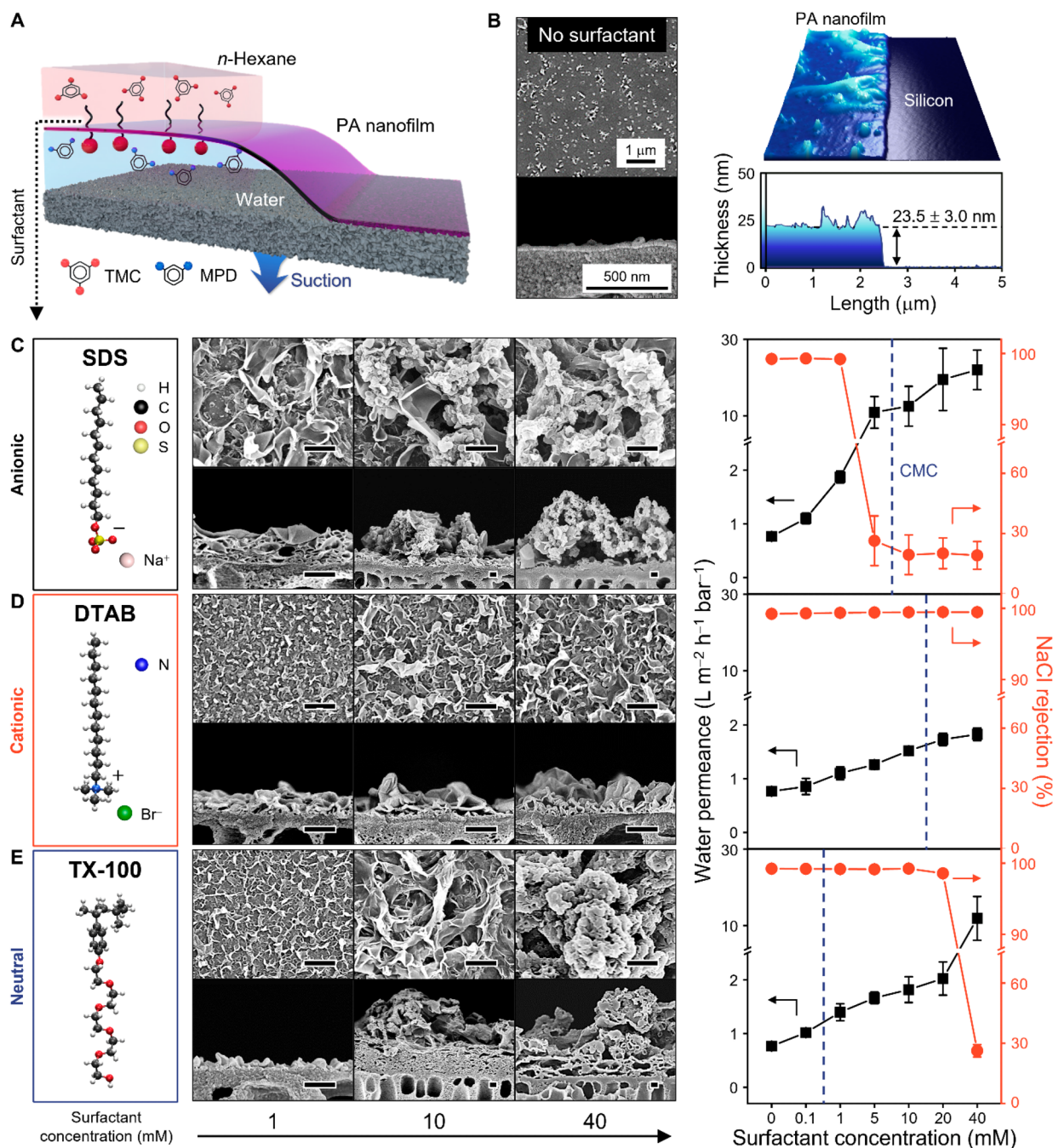


Figure 1. Morphology and separation performance of polyamide (PA) nanofilms synthesized via support-free interfacial polymerization (SFIP) with different surfactants. (A) Schematic illustration of the SFIP process. (B) Scanning electron microscope (SEM) top and cross-sectional and atomic force microscope (AFM) topological images of the PA nanofilm synthesized with no surfactant. (C–E) SEM top and cross-sectional images and RO separation performance of the PA nanofilms synthesized with different surfactants, (C) anionic SDS, (D) cationic DTAB, and (E) neutral TX-100, at various surfactant concentrations. Scale bars denote 1 μm and 500 nm for SEM top and cross-sectional images, respectively. The dotted line in separation performance data denotes the critical micelle concentration (CMC) of the respective surfactant.

regulated IP mechanism difficult. These ambiguities stem from the ill-defined interference of the support (e.g., distribution of the monomer concentration and the shape/uniformity of the reaction interface) in nanofilm formation via conventional IP (Figure S2)^{18,19} and the lack of elaborate characterization tools for capturing a snapshot of the complex and nanoscale IP phenomena.^{1,2}

Here, we identify the inherent surfactant-regulated IP mechanism governing the interfacial formation of PA nanofilms by employing our previously developed support-free IP

(SFIP) technique that can eliminate the support interference¹⁹ and *in situ* visualizing the interfacial phenomena. In SFIP, a freestanding PA nanofilm is assembled at the free interface between MPD aqueous and TMC organic solutions, followed by attachment to a porous support (Figure 1A and Figure S1B). SFIP allows us to focus on analyzing only the effect of the surfactant on interfacial film formation and thus identify key structure-regulating factors by excluding the complex interference of the support. A series of representative anionic (sodium dodecyl sulfate, SDS), cationic (dodecyltrimethylam-

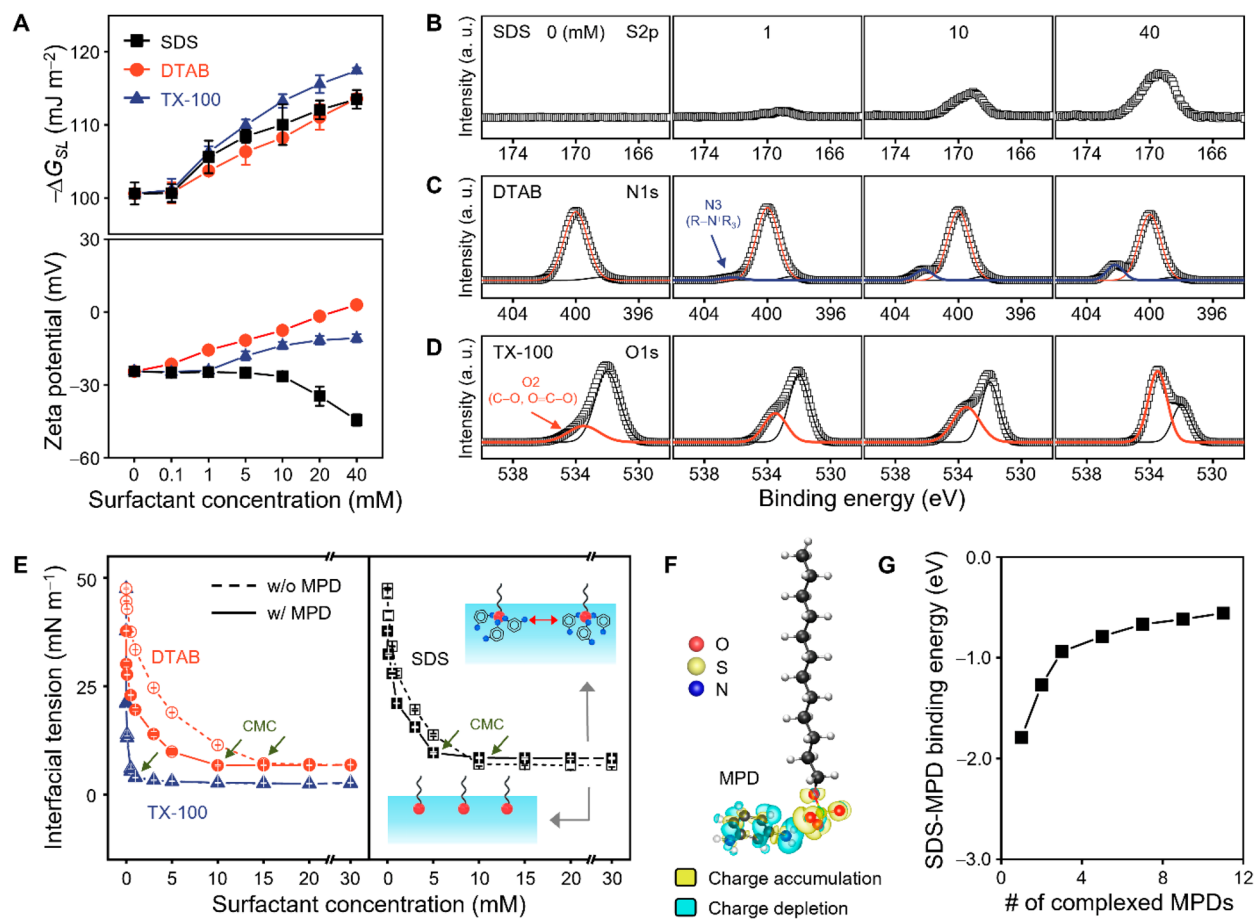


Figure 2. Physicochemical properties of PA nanofilms prepared via SFIP and the molecular configurations of surfactants in the interfacial polymerization process. (A) Intrinsic surface hydrophilicity (solid–liquid interfacial free energy, $-\Delta G_{sl}$) and surface ζ potential of the PA nanofilms prepared with different surfactants at various surfactant concentrations. (B–D) High-resolution XPS (B) sulfur (S 2p), (C) nitrogen (N 1s), and (D) oxygen (O 1s) spectra of the PA nanofilms prepared with SDS, DTAB, and TX-100, respectively, at various surfactant concentrations. (E) Aqueous–organic (*n*-hexane) interfacial tension of surfactant aqueous solutions with or without MPD (2 w/v %) as a function of surfactant concentrations. Green arrows represent CMC values. Inset images represent the SDS molecular configuration at the interface of the equilibrium state when MPD is coexistent (upper) or absent (lower) in water. (F) Charge density difference of the SDS-MPD complex obtained from DFT calculations. The isosurface level is $0.001 \text{ e } \text{\AA}^{-3}$. (G) SDS-MPD binding energy per MPD as a function of the number of complexed MPD molecules.

monium bromide, DTAB), and neutral (Triton X-100, TX-100) surfactants (Table S1) at different concentrations were added to the MPD solution during SFIP to characterize the assembled PA nanofilms (Figure 1B–E). Surfactants with relatively long alkyl chains were selected to clearly identify the surfactant effect (Figure S3).²⁰

A pristine PA nanofilm assembled without any surfactant exhibited a nanoscale thickness ($\sim 24 \text{ nm}$) with small nodular surface features (Figure 1B and Figures S4 and S5), a dense structure with low molecular weight cut-off (MWCO, 84.7 g mol^{-1}) (Figure S6), and good RO performance (NaCl rejection = $99.2 \pm 0.1\%$, water permeance = $0.77 \pm 0.05 \text{ L m}^{-2} \text{ h}^{-1} \text{ bar}^{-1}$). The structure and RO performance of the PA nanofilms were sensitively regulated by adding surfactants depending on the surfactant charge characteristics (Figure 1C–E). Meanwhile, regardless of the surfactant type, surfactant addition enabled the assembly of the ultra-permselective PA nanofilm with ~ 2.4 -fold higher water permeance and intact NaCl rejection compared to the pristine film, albeit at different optimum surfactant concentrations. The addition of anionic SDS led to the most significant change in film structure and performance, producing a highly rough and

multilayered porous PA structure (Figure 1C and Figures S4 and S7). Higher SDS concentrations progressively increased film surface roughness while producing a highly crumpled leaf-like structure (up to 1 mM SDS), which turned into a discrete and aggregated structure at SDS $> 1 \text{ mM}$. This morphological change was accompanied by a drastic increase in the structural hierarchy, apparent thickness, internal void fraction, and backside porosity of the PA nanofilm (Figures S4 and S7). Meanwhile, a noticeable reduction in its NaCl rejection but an increase in its water permeance were observed at SDS $> 1 \text{ mM}$ (Figure 1C), where discrete PA aggregates began to appear. The evolution of the defective aggregates at SDS $> 1 \text{ mM}$ was closely related to the significant reduction in PA density and thus NaCl rejection, as evidenced by its unmeasurably high MWCO (Figure S6). Notably, no enhancement in the molecular density and salt rejection of the PA nanofilm was observed upon the SDS addition (Figure S6). This result provides important insights into the surfactant-regulated IP mechanism; previous observations on the salt rejection enhancement of conventionally IP-assembled PA nanofilms by surfactant (e.g., SDS) addition resulted mainly from the enhanced support wettability rather than the promoted

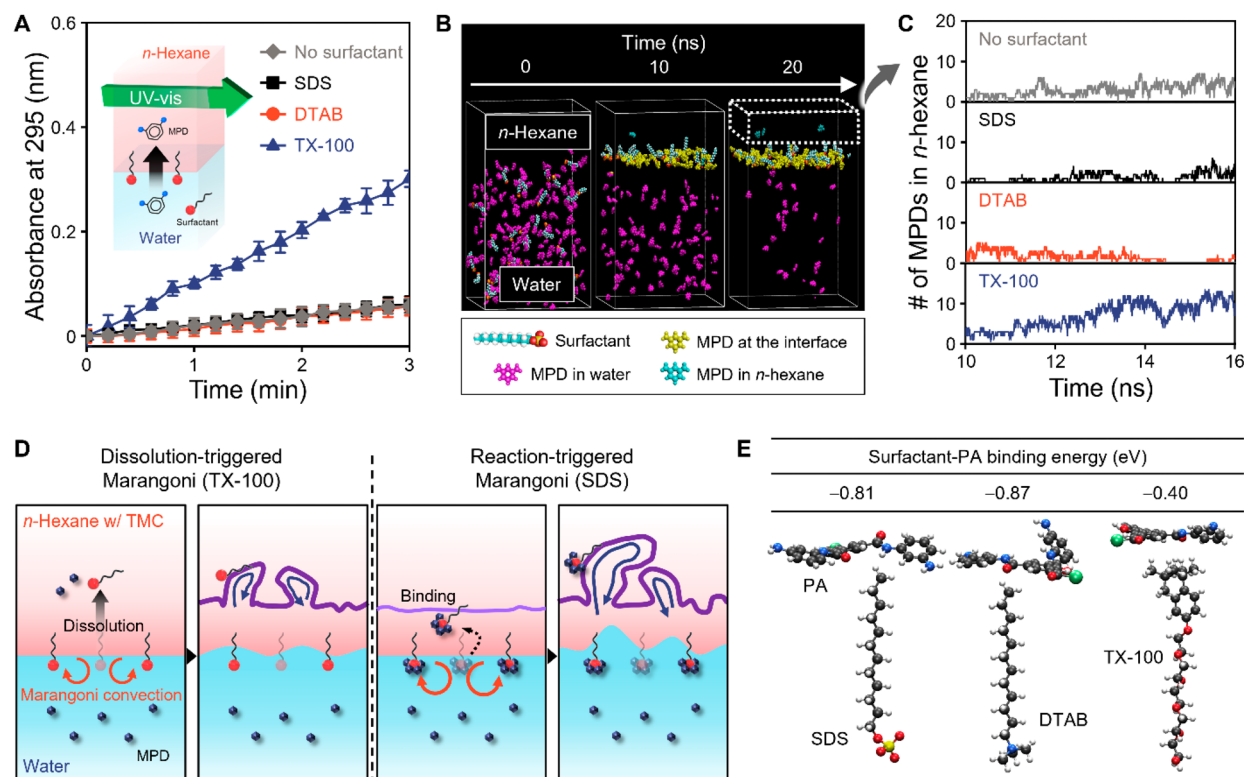


Figure 3. Effect of surfactants on MPD diffusion and related IP mechanism. (A) Characteristic UV-vis absorbance (at 295 nm) of MPD in *n*-hexane which was in contact with an MPD (2 w/v %) aqueous solution containing different surfactants (10 mM) as a function of time. The inset represents a UV-vis experimental setup where the UV-vis light passes through *n*-hexane. (B) Representative MD-simulated snapshots of MPD migration to *n*-hexane from water containing SDS as a function of time. (C) MD-simulated number of MPD molecules in *n*-hexane which is in contact with an MPD aqueous solution containing different surfactants as a function of time. (D) Proposed mechanism of the interfacial formation of a PA nanofilm when TX-100 (left) or SDS (right) is present at the aqueous-organic interface. (E) DFT-calculated maximum binding energies between the surfactants (tail part) and the PA repeating unit in *n*-hexane and their respective intermolecular configurations.

inherent IP reaction. Combined with its reduced molecular density (Figure S6), the increased surface roughness and (internal/backside) porosity (Figures S4 and S7) of the PA nanofilm assembled at higher SDS concentrations would remarkably increase its water permeance owing to the increased permeation area and gutter effect.^{21–23}

In contrast, the addition of cationic DTAB was the least effective at inducing changes to the structure and performance of the PA nanofilm (Figure 1D and Figure S8). Although the crumpled leaf-like feature of the PA nanofilm became pronounced at higher DTAB concentrations, the increase in its surface roughness, thickness, and internal/backside porosity was much less than that for the nanofilms assembled with SDS. Furthermore, unlike SDS, DTAB maintained the PA molecular density estimated by MWCO over the entire surfactant concentration (Figure S9). Consistently, the NaCl rejection of the PA nanofilm remained unchanged as the DTAB concentration increased, even above its critical micelle concentration (CMC), while its water permeance gradually increased due to the evolution of water-permeable structural features (Figure 1D and Figure S8).

The morphology and performance trend of the PA nanofilm assembled with neutral TX-100 was similar to that of the film synthesized with SDS, but less significant (Figure 1E and Figure S10). Moreover, the surfactant concentration above which the PA density and NaCl rejection started to noticeably decrease along with generating the aggregate morphology was

higher for TX-100 (10 mM, above CMC) than for SDS (1 mM, below CMC) (Figure 1E and Figure S11).

Incrementally adding the surfactants also gradually enhanced the surface hydrophilicity (i.e., solid-liquid interfacial free energy, $-\Delta G_{SL}$) of the PA nanofilm while altering its surface charge (i.e., ζ potential) depending on the surfactant type (Figure 2A and Figure S12). The inherent negative surface charge of the PA nanofilm became more pronounced upon the addition of anionic SDS (>10 mM). In contrast, the addition of cationic DTAB and neutral TX-100 gradually attenuated the PA negative surface charge, although DTAB led to greater attenuation. These observations suggest that the surfactants, even at low concentrations, were incorporated into the PA nanofilm during the IP reaction,^{15,21} which was further confirmed by X-ray photoelectron spectroscopy (XPS). A high-resolution XPS analysis revealed that increasing SDS and DTAB concentrations continuously intensified the characteristic peaks of SDS and DTAB at 169.0 (S 2p, sulfur) and 402.2 eV (N3 of N 1s, quaternary ammonium), respectively, which were absent for the pristine PA film (Figure 2B,C and Figures S13 and S14). Furthermore, the incremental addition of TX-100 with an ether-group-rich head progressively increased the peak intensity at 533.5 eV (O2 of O 1s, ether) (Figure 2D and Figure S15).

The IP reaction is characterized as a diffusion-controlled process.^{1,2} MPD aqueous monomers diffuse to the organic phase and react with TMC in the vicinity of the interface to form a nascent PA layer, which decelerates subsequent MPD

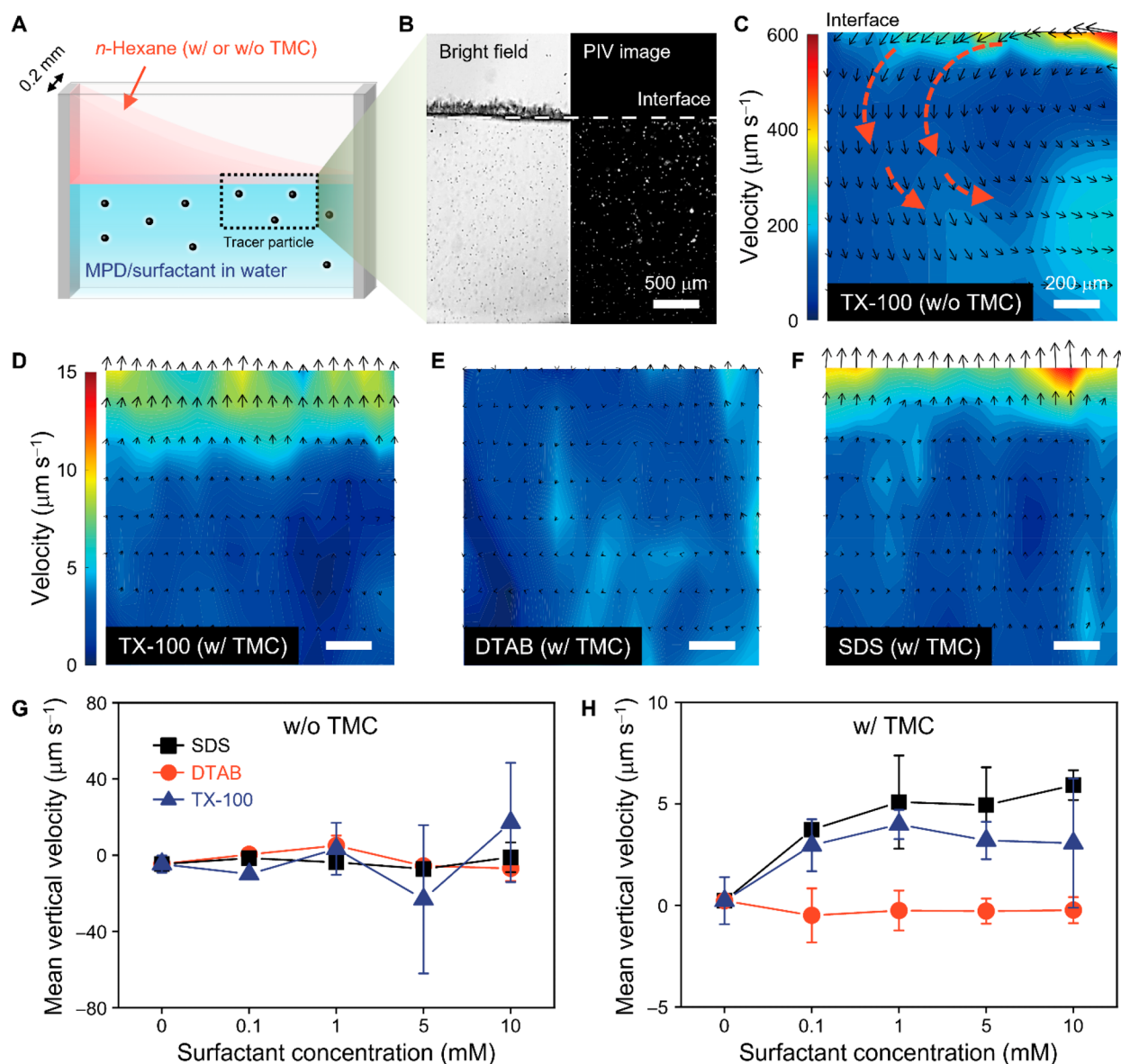


Figure 4. Characterization of the interfacial fluid motion during PA nanofilm formation. (A) Schematic of a Hele–Shaw microfluidics channel to visualize the fluid motion near the aqueous–organic interface by monitoring tracer particles in water when *n*-hexane with or without TMC (0.1 w/v %) was spread onto an MPD (2.0 w/v %)/surfactant (10 mM) aqueous solution. (B) Snapshots of collected bright field (left) and particle image velocimetry (PIV) (right) images. (C–F) Flow fields under the aqueous–organic interfaces formed (C) between *n*-hexane and an MPD aqueous solution containing TX-100 and (D–F) between *n*-hexane with TMC and MPD aqueous solutions containing different surfactants, (D) TX-100, (E) DTAB, and (F) SDS. Black arrows indicate velocity vectors, and contours represent the velocity magnitude. The interface is located at the upper boundary. (G, H) Mean vertical velocity of the aqueous phase flow under the aqueous–organic interfaces formed between *n*-hexane (G) without or (H) with TMC and MPD aqueous solutions containing different surfactants as a function of surfactant concentrations. The vertical flow (+, upward; –, downward) velocity was calculated from the interfacial region within a depth of 250 μm and averaged for 1 s after the interface was completely covered by the *n*-hexane solution.

diffusion, producing an ultrathin PA film (Figure S16A). To elucidate the effect of interfacial tension on the IP mechanism, we characterized the aqueous–organic interfacial tension of the surfactant aqueous solutions with or without MPD as a function of surfactant concentrations (Figure 2E). TX-100 produced a greater reduction in interfacial tension than the other surfactants due to its higher hydrophobicity that stabilizes the interface more effectively.²⁴ The presence of MPD (2 w/v %) in water further reduced interfacial tension and CMC due to the cooperative action of its surface-active property (Figure S17),²¹ which was noticeable for SDS and DTAB. No distinct difference in interfacial tension between

the SDS and DTAB solutions indicates that interfacial tension cannot solely explain the significant differences in the structure and performance of the PA nanofilms assembled with SDS and DTAB. Interestingly, the presence of MPD led to a discernible increase in equilibrium interfacial tension above CMC for SDS, whereas no increase in equilibrium interfacial tension was observed for DTAB and TX-100 (Figure 2E and Figure S18). This can be attributed to strong complexation between SDS and MPD molecules, which destabilizes the interface by inducing steric hindrance (Figure 2E, inset, and Figure S17).²⁵ The anionic sulfate head group of SDS can be complexed with the amine groups of MPD via strong electrostatic and ion–

dipole interactions.²⁶ Density functional theory (DFT) calculations revealed that MPD has a significantly higher binding energy with SDS ($E_b = -1.86$ eV) than with DTAB and TX-100 (-0.29 eV) (Figure 2F and Figure S19). Although the SDS-MPD binding energy decreases progressively with the increasing number of complexed MPD molecules, the binding energy is still highly attractive (Figure 2G), suggesting that multiple MPD molecules can be bound to a single SDS molecule (Figure S20).

We also used UV-visible spectroscopy to investigate the influence of surfactants on MPD diffusion by monitoring the time-varying amount of MPD in *n*-hexane, to which MPD diffused from water (Figure 3A and Figure S21). The addition of SDS and DTAB to water did not distinctly enhance MPD diffusion to *n*-hexane, suggesting that the surfactant-induced reduction of interfacial tension does not guarantee the enhancement of MPD diffusion during the IP reaction. In contrast, TX-100 present in water remarkably enhanced MPD migration to *n*-hexane. Meanwhile, relatively hydrophobic TX-100 noticeably dissolved into *n*-hexane (i.e., relatively high oil-water partition coefficient ($P_{o/w}$)), unlike highly hydrophilic ionic SDS and DTAB (i.e., negligible $P_{o/w}$) (Table S1).²⁷ These experimental results were verified by molecular dynamic (MD) simulations to quantify the number of MPD molecules that diffuse from water toward *n*-hexane across the interface with time (Figure 3B,C). Consistently, the addition of SDS and DTAB led to no noticeable increase in the number of diffusing MPD molecules, unlike TX-100, which notably enhanced MPD diffusion (Figure 3C and Figure S22).

Because IP is a complex process involving the simultaneous diffusion and reaction of various molecules, the nanofilm formed via IP is susceptible to interfacial instabilities via various mechanisms, possibly producing an irregular film structure.^{1,10,23,28} Specifically, the spontaneous dissolution of highly surface-active TX-100 into *n*-hexane can create its concentration inhomogeneity and thus an interfacial tension gradient along the interface. This non-uniform interfacial tension drives liquid motion along the interface toward regions with higher interfacial tension, which sets the underlying liquid in motion, inducing a convective interfacial flow, called solutal Marangoni convection.^{24,28,29} The interfacial turbulent flow induced by Marangoni instability presumably provoked the crumpling of the initially formed nascent PA layer while promoting the trans-interface migration of MPD monomers (Figure 3D and Figure S16B; see text in the Supporting Information).^{11,28,30} The continuous MPD diffusion-reaction coupled with successive film crumpling likely resulted in a rough, thick, and multi-layered porous PA nanofilm.^{1,2} Although the heat released from the exothermic IP reaction possibly drives Rayleigh-Benard instability,¹⁰ this thermally-driven instability may not dominate the Marangoni effect due to the small Rayleigh number.¹⁶ Interfacial degassing may partially contribute to the interfacial instability, but its effect may also not be strong in our case. This is because generated nanobubbles can be effectively eliminated when PA nanofilms are formed at the free interface.²³ Excessive interfacial fluctuations produced at high TX-100 concentrations (>10 mM) could generate a Marangoni stress high enough to rupture and fragment the nascent PA layer, yielding a more irregular and defective PA structure (Figure 1E).¹ Meanwhile, significantly accelerated MPD diffusion could further contribute to the formation of the defective PA nanofilm by unbalancing reactant stoichiometry.¹⁴

The question arises as to how SDS can alter the structure and performance of the PA nanofilm to a greater extent than TX-100. Considering interfacial phenomena during the IP reaction, the surfactants located at the interface are expected to strongly interact with the nascent PA film formed in *n*-hexane through various interactions.^{15,21} DFT calculations revealed that many possible intermolecular configurations between the surfactants and the PA exhibited favorable binding energies in *n*-hexane (Figure S23), which likely enabled the incorporation of the surfactants into the PA (Figure 2A-D). Particularly, the tail part of the surfactant would more dominantly interact with the PA layer via a hydrophobic interaction due to spatial proximity (Figure 3E).¹⁵ Hence, one can reasonably postulate that although the trans-interface transfer of SDS and DTAB to *n*-hexane is not inherently allowed without the IP reaction, it is enabled when the surfactants are bound to the nascent PA layer formed in *n*-hexane by the initial IP reaction. This reaction-induced migration of the surfactants to *n*-hexane presumably triggered Marangoni instability by generating the interfacial tension gradient,²⁸ consequently crumpling the nascent PA film while promoting MPD diffusion (Figure 3D and Figure S16C). Specifically, the trans-interface migration of SDS complexed with many surface-active MPD molecules may cause the catastrophic local fluctuation of interfacial tension, inducing significant Marangoni instability. This plausible hypothesis can account for the greater structural and performance change of the PA nanofilm assembled with SDS than those assembled with non-complexing DTAB and TX-100 (see text in the Supporting Information). Particularly, non-complexing DTAB that does not dissolve into *n*-hexane was responsible for the lack of change in the PA structure because it would induce the least Marangoni instability.³¹

To demonstrate our hypothesis, we *in situ* monitored the fluid motion of the aqueous phase near the interface formed when *n*-hexane with or without TMC was spread onto an MPD/surfactant aqueous solution containing tracer particles (Figure 4, Figures S24 and S25, and Movies S1-10). When pure *n*-hexane was spread from left to right, TX-100 in water induced a strong circulating flow opposite to the spreading direction under the interface (Figure 4C and Movie S6), unlike SDS and DTAB (Figure S26 and Movies S4 and S5). This result demonstrates chemo-Marangoni convection driven by the dissolution of TX-100 into *n*-hexane. The solutal Marangoni effect of TX-100 was also reflected by a large variation in the mean vertical flow velocity, which became more pronounced at higher TX-100 concentrations due to intensified Marangoni instability (Figures 4G and Figure S27). When *n*-hexane with TMC was used to induce the IP reaction, the overall interfacial flow (in particular, the horizontal flow component) was dampened, presumably due to interfacial resistance imposed by a forming PA nanofilm.²⁴ Nevertheless, the vertical interfacial flow was still prominent (Figure 4D, Figure S28, and Movie S10), implying that the Marangoni flow induced by TX-100 vertically pushes upward on the interfacial fluid, thus crumpling a PA nanofilm (Figure 3D, left). Interestingly, the IP reaction remarkably reinforced the vertical interfacial flow of the SDS-containing water, whose magnitude was higher than that of DTAB and even TX-100 (Figure 4D-F, Figure S28, and Movies S8-10), confirming the significant reaction-triggered Marangoni effect for complexing SDS (Figure 3D, right). As the surfactant concentration increased, the mean vertical flow velocity notably increased for SDS and TX-100 due to the enhanced driving force for Marangoni

instability (Figure 4H and Figure S29).^{24,31} Although the Marangoni instability driven by SDS and TX-100 significantly distorted the PA nanofilm, the vigorous trans-interface transport of MPD reactants complexed with SDS likely deformed the PA film structure to a greater extent by intensifying the IP reaction.¹⁴

To further verify our hypothesis, we extended our study to another set of anionic (sodium lauroyl sarcosinate, SLAS), cationic (hexadecyltrimethylammonium bromide, CTAB), and neutral (Tergitol TMN-10, TMN-10) surfactants (Table S2). Consistently, anionic SLAS caused the most significant change in the structure and performance of the PA nanofilm (Figures S30–S32), followed by TMN-10 (Figures S32–S34) and CTAB (Figures S32, S35, and S36). All surfactants altered the film properties by being incorporated into the PA (Figures S37–S39). Like SDS, anionic SLAS only exhibited increased equilibrium interfacial tension when MPD was present in water (Figure S40). Consistently, MPD had a much higher binding energy with SLAS than with CTAB and TMN-10 via electrostatic and ion–dipole interactions (Figure S41), which enabled the complexation of SLAS with multiple MPD molecules (Figure S42). Furthermore, neutral non-ionic TMN-10 only noticeably promoted MPD diffusion (Figure S43) while dissolving into *n*-hexane (i.e., high $P_{o/w}$) (Table S2). Similar to TX-100, TMN-10 present in water generated interfacial convection under the aqueous–organic interface upon contact with pure *n*-hexane due to the dissolution-triggered Marangoni effect (Figures S44 and S45), significantly distorting the PA structure. In contrast, ionic SLAS and CTAB induced no strong interfacial flow with pure *n*-hexane (Figures S44 and S45). Nevertheless, because all surfactants favorably interact with PA (Figure S46), the IP reaction triggered Marangoni convection by allowing the surfactants to adhere to the nascent PA film. Like SDS, complexing SLAS caused a significant Marangoni flow (Figures S45 and S47) while enabling the trans-interface migration of surplus complexed MPDs, consequently altering the film structure and performance to a greater extent than non-complexing CTAB and even dissoluble TMN-10. Consistent results were further observed for the third set of surfactants (Figure S48).

Here, PA nanofilm membranes were assembled at the free interface in the presence of differently charged surfactants to elucidate the role of surfactants in the interfacial formation of the nanofilms. We discovered that surfactants regulated the IP mechanism and thus the resultant film structure and performance by triggering solutal Marangoni instability via different mechanisms (i.e., surfactant dissolution, surfactant binding to reaction products, and/or surfactant–reactant complexation) depending on the surfactant charge. Particularly, the surfactant that can be strongly complexed with reactants induced significant reaction-triggered Marangoni instability, consequently altering the film structure and performance to a greater extent than non-complexing surfactants. Nevertheless, the delicate control of the surfactant concentration enabled the fabrication of highly cross-linked, ultra-permeable nanomembranes for desalination and water purification regardless of the surfactant type. Specifically, the surfactant that triggered a greater Marangoni instability needed to be used in a less amount to achieve optimal performance. From a fundamental perspective, our study significantly improved our understanding of the surfactant-regulated IP process by providing a convincing mechanism. From a practical perspective, our findings provide key knowledge on

how the surfactant structure (i.e., charge characteristics) determines the Marangoni-triggering mechanism and thus regulates the IP process. This knowledge is useful for rationally tailoring the structure and properties of various polymer nanofilms synthesized via surfactant-regulated interfacial reactions by allowing us to properly use surfactants. As future research, it is desirable to identify the effect of other structural characteristics of surfactants (e.g., tail chain length, counterion type, and head group chemistry) on interfacial nanofilm formation, particularly in the presence of supports.

■ ASSOCIATED CONTENT

SI Supporting Information

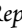
The Supporting Information is available free of charge at <https://pubs.acs.org/doi/10.1021/acs.nanolett.3c00374>.


Materials, experimental procedures, characterization methods, computational methods, supporting text, additional SEM and AFM images, attenuated total reflectance Fourier transform infrared data, XPS data, additional computational data, and additional PIV data (PDF)


Bright field and PIV movies (ZIP)

■ AUTHOR INFORMATION

Corresponding Authors

Hyoungsoo Kim – Department of Mechanical Engineering, Korea Advanced Institute of Science and Technology, Daejeon 34141, Republic of Korea;  orcid.org/0000-0002-2393-723X; Email: hshk@kaist.ac.kr

Kwang-Ryeol Lee – Computational Science Research Center, Korea Institute of Science and Technology, Seoul 02792, Republic of Korea; On leave at the Department of Chemistry, Uppsala University, Uppsala 75105, Sweden;  orcid.org/0000-0002-8211-3257; Email: krlee@kist.re.kr

Jung-Hyun Lee – Department of Chemical and Biological Engineering, Korea University, Seoul 02841, Republic of Korea;  orcid.org/0000-0002-9662-1703; Email: leejhyyy@korea.ac.kr


Authors

Sung-Joon Park – Department of Chemical and Biological Engineering, Korea University, Seoul 02841, Republic of Korea

Myung-Seok Lee – Department of Chemical and Biological Engineering, Korea University, Seoul 02841, Republic of Korea

Mehmet Emin Kilic – Computational Science Research Center, Korea Institute of Science and Technology, Seoul 02792, Republic of Korea; Present Address: Department of Physics, Virginia Commonwealth University, Richmond, Virginia 23284, United States

Junil Ryu – Department of Mechanical Engineering, Korea Advanced Institute of Science and Technology, Daejeon 34141, Republic of Korea

Hosik Park – Green Carbon Research Center, Chemical and Process Technology Division, Korea Research Institute of Chemical Technology, Daejeon 34114, Republic of Korea;  orcid.org/0000-0002-5151-1113

You In Park – Green Carbon Research Center, Chemical and Process Technology Division, Korea Research Institute of Chemical Technology, Daejeon 34114, Republic of Korea

Complete contact information is available at:

<https://pubs.acs.org/10.1021/acs.nanolett.3c00374>

Author Contributions

[#]S.-J.P., M.-S.L., M.E.K., and J.R. contributed equally. Conceptualization: J.-H.L., K.-R.L., H.K. Data curation: S.-J.P., M.-S.L., M.E.K., J.R. Formal analysis: S.-J.P., M.-S.L., M.E.K., J.R. Funding acquisition: J.-H.L., K.-R.L., H.K. Investigation: J.-H.L., K.-R.L., H.K., S.-J.P., M.-S.L., M.E.K., J.R. Methodology: S.-J.P., M.-S.L., M.E.K., J.R., H.P., Y.I.P. Project administration: J.-H.L., K.-R.L., H.K. Supervision: J.-H.L., K.-R.L., H.K. Validation: J.-H.L., K.-R.L., H.K., S.-J.P., M.-S.L., M.E.K., J.R. Visualization: S.-J.P., M.-S.L., M.E.K., J.R. Writing—original draft: S.-J.P., M.-S.L., M.E.K., J.R. Writing—review and editing: J.-H.L., K.-R.L., H.K.

Notes

The authors declare no competing financial interest.

ACKNOWLEDGMENTS

This research was supported by the National Research Foundation of Korea (NRF) grant funded by the Korean government (2023R1A2C2002913, 2022R1A5A1032539, 2021R1A2C2007835, 2020H1D3A1A02081517, and KK2311-40).

REFERENCES

- (1) Freger, V.; Ramon, G. Z. Polyamide Desalination Membranes: Formation, Structure, and Properties. *Prog. Polym. Sci.* **2021**, *122*, 101451.
- (2) Wang, Z.; Liang, S.; Kang, Y.; Zhao, W.; Xia, Y.; Yang, J.; Wang, H.; Zhang, X. Manipulating Interfacial Polymerization for Polymeric Nanofilms of Composite Separation Membranes. *Prog. Polym. Sci.* **2021**, *122*, 101450.
- (3) Chung, J. Y.; Nolte, A. J.; Stafford, C. M. Surface Wrinkling: a Versatile Platform for Measuring Thin-Film Properties. *Adv. Mater.* **2011**, *23*, 349–368.
- (4) Scriven, L. E.; Sternling, C. V. The Marangoni Effects. *Nature* **1960**, *187*, 186–188.
- (5) Chowdhury, M. R.; Steffes, J.; Huey, B. D.; McCutcheon, J. R. 3D Printed Polyamide Membranes for Desalination. *Science* **2018**, *361*, 682–686.
- (6) Elimelech, M.; Phillip, W. A. The Future of Seawater Desalination: Energy, Technology, and the Environment. *Science* **2011**, *333*, 712–717.
- (7) Geise, G. M. Why Polyamide Reverse-Osmosis Membranes Work So Well. *Science* **2021**, *371*, 31–32.
- (8) Werber, J. R.; Osuji, C. O.; Elimelech, M. Materials for Next-Generation Desalination and Water Purification Membranes. *Nat. Rev. Mater.* **2016**, *1*, 16018.
- (9) Tan, Z.; Chen, S.; Peng, X.; Zhang, L.; Gao, C. Polyamide Membranes with Nanoscale Turing Structures for Water Purification. *Science* **2018**, *360*, 518–521.
- (10) Karan, S.; Jiang, Z.; Livingston, A. G. Sub-10 nm Polyamide Nanofilms with Ultrafast Solvent Transport for Molecular Separation. *Science* **2015**, *348*, 1347–1351.
- (11) Li, B.; Japip, S.; Chung, T.-S. Molecularly Tunable Thin-Film Nanocomposite Membranes with Enhanced Molecular Sieving for Organic Solvent Forward Osmosis. *Nat. Commun.* **2020**, *11*, 1198.
- (12) Liang, Y.; Zhu, Y.; Liu, C.; Lee, K.-R.; Hung, W.-S.; Wang, Z.; Li, Y.; Elimelech, M.; Jin, J.; Lin, S. Polyamide Nanofiltration Membrane with Highly Uniform Sub-Nanometre Pores for Sub-1 Å Precision Separation. *Nat. Commun.* **2020**, *11*, 2015.
- (13) Nulens, I.; Zvi, A. B.; Vankelecom, I. F. J.; Ramon, G. Z. Re-Thinking Polyamide Thin Film Formation: How Does Interfacial Destabilization Dictate Film Morphology? *J. Membr. Sci.* **2022**, *656*, 120593.
- (14) Klaysom, C.; Hermans, S.; Gahlaut, A.; Craenenbroeck, S. V.; Vankelecom, I. F. J. Polyamide/Polyacrylonitrile (PA/PAN) Thin Film Composite Osmosis Membranes: Film Optimization, Characterization and Performance Evaluation. *J. Membr. Sci.* **2013**, *445*, 25–33.
- (15) Mansourpanah, Y.; Madaeni, S. S.; Rahimpour, A. Fabrication and Development of Interfacial Polymerized Thin-Film Composite Nanofiltration Membrane Using Different Surfactants in Organic Phase; Study of Morphology and Performance. *J. Membr. Sci.* **2009**, *343*, 219–228.
- (16) Dennison, J. M.; Xie, X.; Murphy, C. J.; Cahill, D. G. Density, Elastic Constants, and Thermal Conductivity of Interfacially Polymerized Polyamide Films for Reverse Osmosis Membranes. *ACS Appl. Nano Mater.* **2018**, *1*, 5008–5018.
- (17) Li, X.; Wang, Z.; Han, X.; Liu, Y.; Wang, C.; Yan, F.; Wang, J. Regulating the Interfacial Polymerization Process toward High-Performance Polyamide Thin-Film Composite Reverse Osmosis and Nanofiltration Membranes: a Review. *J. Membr. Sci.* **2021**, *640*, 119765.
- (18) Ghosh, A. K.; Hoek, E. M. V. Impacts of Support Membrane Structure and Chemistry on Polyamide-Polysulfone Interfacial Composite Membranes. *J. Membr. Sci.* **2009**, *336*, 140–148.
- (19) Park, S.-J.; Choi, W.; Nam, S.-E.; Hong, S.; Lee, J. S.; Lee, J.-H. Fabrication of Polyamide Thin Film Composite Reverse Osmosis Membranes via Support-Free Interfacial Polymerization. *J. Membr. Sci.* **2017**, *526*, 52–59.
- (20) Aidarova, S.; Sharipova, A.; Krägel, J.; Miller, R. Polyelectrolyte/Surfactant Mixtures in the Bulk and at Water/Oil Interfaces. *Adv. Colloid Interface Sci.* **2014**, *205*, 87–93.
- (21) Park, S.-J.; Lee, M.-S.; Choi, W.; Lee, J.-H. Biocidal Surfactant-Assisted Fabrication of Thin Film Composite Membranes with Excellent and Durable Anti-Biofouling Performance. *Chem. Eng. J.* **2022**, *431*, 134114.
- (22) Zhang, Z.; Qin, Y.; Kang, G.; Yu, H.; Jin, Y.; Cao, Y. Tailoring the Internal Void Structure of Polyamide Films to Achieve Highly Permeable Reverse Osmosis Membranes for Water Desalination. *J. Membr. Sci.* **2020**, *595*, 117518.
- (23) Gan, Q.; Peng, L. E.; Yang, Z.; Sun, P.-F.; Wang, L.; Guo, H.; Tang, C. Y. Demystifying the Role of Surfactant in Tailoring Polyamide Morphology for Enhanced Reverse Osmosis Performance: Mechanistic Insights and Environmental Implications. *Environ. Sci. Technol.* **2023**, *57*, 1819–1827.
- (24) Agble, D.; Mendes-Tassis, M. A. The Prediction of Marangoni Convection in Binary Liquid-Liquid Systems with Added Surfactants. *Int. J. Heat Mass Transf.* **2001**, *44*, 1439–1449.
- (25) Tan, J.; Xiong, X.; He, Z.; Cao, F.; Sun, D. Aggregation Behavior of Polyether Based Siloxane Surfactants in Aqueous Solutions: Effect of Alkyl Group and Steric Hindrance. *J. Phys. Chem. B* **2019**, *123*, 1390–1399.
- (26) Penfold, J.; Thomas, R. K.; Zhang, X. L.; Taylor, D. J. F. Nature of Amine-Surfactant Interactions at the Air-Solution Interface. *Langmuir* **2009**, *25*, 3972–3980.
- (27) Pollard, J. M.; Shi, A. J.; Göklen, K. E. J. Solubility and Partitioning Behavior of Surfactants and Additives Used in Bioprocesses. *Chem. Eng. Data* **2006**, *51*, 230–236.
- (28) Sternling, C. V.; Scriven, L. E. Interfacial Turbulence: Hydrodynamic Instability and the Marangoni Effect. *AIChE J.* **1959**, *5*, 514–523.
- (29) Slavtchev, S.; Kalitzova-Kurteva, P.; Mendes, M. A. Marangoni Instability of Liquid-Liquid Systems with a Surface-Active Solute. *Colloids Surf. A Physicochem. Eng. Asp.* **2006**, *282*, 37–49.
- (30) Kim, H.; Muller, K.; Shardt, O.; Afkhami, S.; Stone, H. A. Solutal Marangoni Flows of Miscible Liquids Drive Transport without Surface Contamination. *Nat. Phys.* **2017**, *13*, 1105–1110.
- (31) Dunér, G.; Kim, M.; Tilton, R. D.; Garoff, S.; Przybycien, T. M. Effect of Polyelectrolyte-Surfactant Complexation on Marangoni Transport at a Liquid-Liquid Interface. *J. Colloid Interface Sci.* **2016**, *467*, 105–114.